applied optics

Eliminating the middleman: ultraviolet scale realization using a laser-driven plasma light source

Uwe Arp,* Edward Hagley, and Robert Vest

Ultraviolet Radiation Group, Sensor Science Division, Physical Measurement Laboratory, National Institute of Standards and Technology, 100 Bureau Dr., Gaithersburg, Maryland 20899, USA
Corresponding author: uwe.arp@nist.gov

After we replaced the argon mini-arc with a laser-driven light source in the Ultraviolet Spectral Comparator Facility at the National Institute of Standards and Technology (NIST), we realized that the optical power should be sufficient to use the comparator system for absolute-cryogenic radiometry. Calibrating working standard detectors directly against an absolute-cryogenic radiometer in the system used for calibrations would eliminate all uncertainties resulting from the use of transfer standards, which were calibrated in a separate system using a different light source and optics. The transfer standards are the middlemen we refer to in the title. Any uncertainty caused by differences in bandpass, out-off-band radiation, spectral purity, collimation, or data interpolation would be removed. In the end, we successfully set up a twin system resembling the Ultraviolet Spectral Comparator Facility and used this system to perform a primary calibration of several photodiodes, based on an absolute-cryogenic radiometer. Using this system, we were able to reduce relative standard uncertainties at wavelengths below 220 nm from above 1 % ($k = 1$) to below 0.5%. We refer to this system as the Ultraviolet Scale Realization Facility or UV-SRF.

https://doi.org/10.1364/AO.414700

1. INTRODUCTION

Over the last 20 years, National Measurement Institutes has moved to use tunable laser systems for scale realization efforts [1,2]. This turned out to be challenging in the ultraviolet spectral region, where lasers needed to be tripled and quadrupled. At NIST, ultraviolet spectral power responsivity calibrations of photodiodes [3] are generally performed in 5 nm steps in the wavelength interval between 200 nm and 400 nm [4]. Multiplied laserlines do not always perfectly match the desired wavelength, and in those cases interpolation has to be used. The differences between the calibration and the scale realization setups lead to increased uncertainties because of dissimilarity in bandpass [5–7], out-of-band stray-light [8], spectral purity, collimation, and the need for interpolation.

Another approach used synchrotron radiation in the ultraviolet spectral region [9–13], which makes perfect sense at wavelengths below 200 nm, but not necessarily in the air-ultraviolet spectral range between 200 nm and 400 nm, since the advent of high-powered laser-driven plasma sources [14–16]. NIST routinely uses such a source in ultraviolet detector calibrations [17,18] since it replaced the argon mini-arc [19–21].

Successful scale realization efforts are based on the accurate measurement of a stable detector's spectral power responsivity

$R(\lambda)$, which is determined by measuring the optical power $P(\lambda)$ incident on the detector and the generated photocurrent $I(\lambda)$ in photovoltaic mode without any bias voltage:

$$R(\lambda) = \frac{I(\lambda)}{P(\lambda)}. \tag{1}$$

In this effort, the optical power measurement relied on an absolute-cryogenic radiometer (ACR) [22–24], a device that revolutionized the accuracy of optical power measurements in radiometry. The ACR is an electrical-substitution radiometer that links radiative power to electrical power measurements. This particular device was operated in constant temperature mode and compared the electrical heating power to the incident radiation. The measurement of the current generated in the photodiodes being calibrated was based on high-accuracy transimpedance amplifiers [25] and low-noise photodiodes [3,26], which are stable under ultraviolet exposure and respond uniformly across their surfaces.

2. EXPERIMENT

This ultraviolet scale realization was based on a laser-driven light source [14–16] and an ACR [22–24]. The laser-generated plasma was imaged onto the circular entrance aperture of a double Czerny–Turner monochromator [27] with a magnification
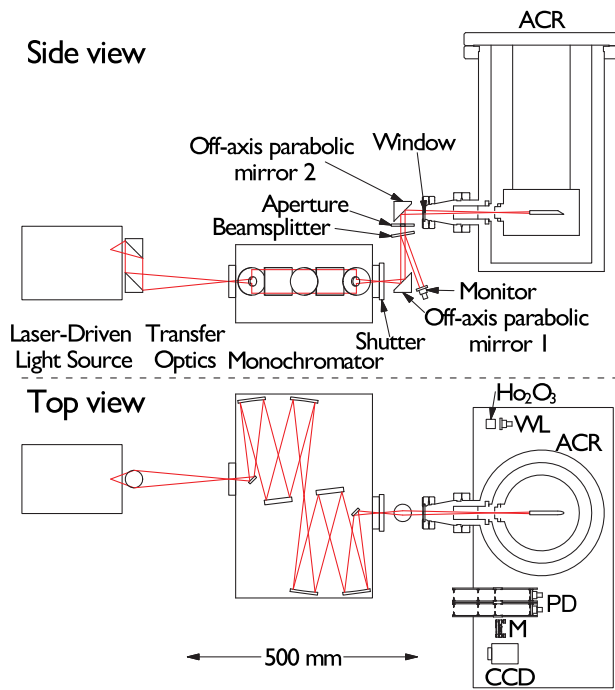
Fig. 1. Layout of the Ultraviolet Scale Realization Facility UV-SRF. In top view, absolute-cryogenic radiometer, **ACR**; plane mirror, **M**; photodiodes, **PD**; charged-coupled device camera, **CCD**; holmium oxide target, **Ho₂O₃**; photodiode for wavelength calibration, **WL**. The platform on the right is mounted on a three-dimensional motion system.

of 4 to match the angular acceptance of the monochromator. The 0.5-mm-diameter circular exit aperture of the monochromator was then magnified fourfold into the measurement system. The imaging was accomplished using two 90° off-axis parabolic (OAP) mirrors, mounted together using mechanical prealignment. This OAP mount was installed on a manually controlled x, y, z-motion stage. The ACR, the detectors-under-test, a 50.8 mm flat mirror for alignment, a CCD camera, and a system for the wavelength calibration were all mounted together on a platform attached to a motorized x, y, z-motion stage to allow for swift and reproducible change between positions (see Fig. 1).

Contributors to the uncertainty of this measurement were the wavelength calibration, window transmission, non-uniformities in the responsivity across the photodiode's surface, accuracy of the positioning, scattered light, the spectral bandwidth of the monochromatized light, the electrical power scale measurement scale factor, the cavity absorptance, the optical-electrical non-equivalence [12], and the noise in the optical power and current measurements.

A. Wavelength Calibration

To achieve sufficient wavelength accuracy, we installed an absolute angular encoder on one of the grating mounts. We then scanned the monochromator over the absorption lines in an aqueous solution of 4% holmium oxide in 10% perchloric acid [28–30]. Using the known wavelength of the different lines, we performed a fit of the grating equation for the Czerny–Turner monochromator using the angular positions of the different
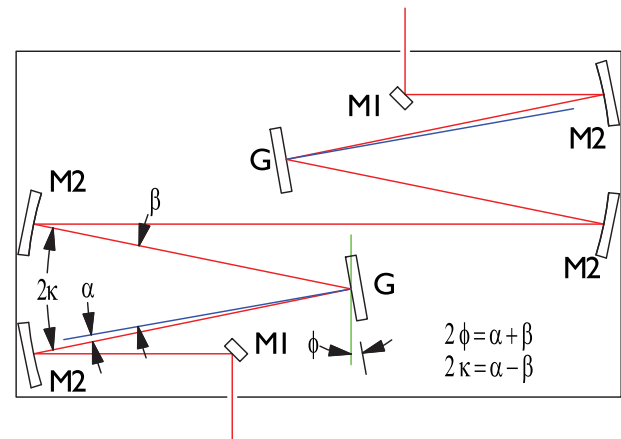

Fig. 2. Sketch of a double Czerny–Turner monochromator with an explanation of the different angles used in Eqs. (2) and (3). **M1**, plane mirrors; **M2**, spherical mirrors; **G**, plane gratings.

lines, which led to parameters to calculate the wavelength from the angular position.

Equation (2) [31] is the grating equation, where α is the angle of incidence relative to the grating normal of the incoming light and β is the angle of reflection relative to the grating normal of the reflected light, m is the diffraction order, λ the wavelength, and d the distance between grooves (see Fig. 2 for details). By convention $m = -1$ for our case, $\alpha \geq 0$, and $\beta \leq 0$ [31],

$$m \cdot \lambda = d \cdot (\sin \alpha + \sin \beta). \tag{2}$$

In Eq. (3) the grating equation has been rewritten for the case of the Czerny–Turner mount [31], using the half-deviation angle κ and the scan angle ϕ. This formulation is more practical, and in our case the scan angle ϕ is measured using the absolute angular encoder,

$$m \cdot \lambda = 2 \cdot d \cdot \cos(\kappa) \cdot \sin(\phi). \tag{3}$$

The angular encoder delivers an angular position in counts, with 2^{32} counts on a full circle. That leads to the following equation for the fitting procedure assuming a grating with a groove spacing of $d = 1200^{-1} \cdot$ mm:

$$y = \frac{2}{1200} \text{mm} \cdot \cos(A) \cdot \sin\left(\frac{x \cdot 2 \cdot \pi}{2^{32} - 1} - B\right), \tag{4}$$

where x represents the encoder counts and y represents the wavelength. A and B are the resulting fit parameters, which will be used to calculate the wavelength from the angular position. The wavelength accuracy of this method can be derived from the uncertainty of the angular measurement. The derivative of Eq. (3) leads to a functional connection between wavelength accuracy $\Delta \lambda$ and the angular resolution $\Delta \phi$ of the encoder:

$$\Delta \lambda = \frac{2 \cdot d}{m} \cdot \cos(\kappa) \cdot \cos(\phi) \Delta \phi. \tag{5}$$

The manufacturer's documentation for the 100-mm-diameter absolute encoder states an angular resolution of $\Delta \phi = 2.86$ arcsec, which is $1.387 \cdot 10^{-5}$ rad. Following [32], the uncertainty of the angle measurement can be estimated to be $\sigma_\phi = 0.5 \cdot \Delta \phi / \sqrt{3} = 4.00 \cdot 10^{-6}$ rad. Using Eq. (5)

with $\kappa = 15°$ and $\phi = -7.136°$, which corresponds to a wavelength of 200 nm, we get an estimated standard uncertainty of $\sigma_\lambda \approx 0.006$ nm for a grating with a groove spacing of $d = 1200^{-1} \cdot$ mm.

The standard uncertainty in the wavelength positions of the different peaks in the holmium oxide absorption target is about 0.1 nm [29,30]. This uncertainty and the accuracy of the measurement of the line position from our data determine the accuracy of the wavelength calibration. We determined the peak positions from the zero crossing of the first derivative of the absorbance data and estimated the standard uncertainty of this process to be 0.2 nm, which led to an estimate of the standard uncertainty in the wavelength scale of ± 0.22 nm.

For the actual measurement, the holmium oxide target was installed on a linear motion stage in front of a silicon photodiode. Then the wavelength of the monochromator was scanned in 0.1 nm steps. At each wavelength, a reading of the background signal of the photodiode with the shutter closed was taken, then the shutter was opened, and a measurement without and with the absorption target in front of the photodiode was recorded. The background was subtracted from the signals, and the absorbance was calculated.

B. Absolute-Cryogenic Radiometer

Initially the ACR [11,12] and the photodiodes were placed in the same vacuum chamber. This way, the light coming from the monochromator had to pass through the same window for measurements of both, which allowed us to ignore the window transmission in the data analysis. The photodiodes were installed in front of the ACR on a vertical translation stage, and the measurement platform was translated longitudinally to perform the diode and ACR measurements at the same distance from the second mirror. However, one significant difference between the measurement of diodes and ACR remained: the photodiodes were much closer to the window than the ACR's cavity. Silicon photodiodes have very high reflectivity in the ultraviolet spectral region [33–36], and even though the window and photodiodes were horizontally tilted to avoid specularly reflected light, the diffuse scattering was strong enough to disturb the incoming light field. So after some discussion, we decided to operate the photodiodes in air, which meant that we had to carefully characterize the window transmission for the data analysis.

The ACR data reduction was based on an algorithm that was developed at NIST. In the example shown in Fig. 3, $N = 40$ data points were collected in each step of the acquisition process. Before the measurement sequence was initiated, the optical shutter was closed. Then N data points were collected as part of the background measurement (step A in Fig. 3). The shutter was opened, and N points were collected while the ACR was settling (step B in Fig. 3). Following this, the actual data were collected (step C in Fig. 3). The shutter was closed again, and in the fourth period the ACR settled again (step D in Fig. 3). Then a second background measurement was done. To determine the optical power, a first-order polynomial was fitted to the background data from steps A and E in Fig. 3. The data from step C in Fig. 3 were subtracted from this linear approximation (step F in Fig. 3), and the mean of the N resulting values was used as the optical
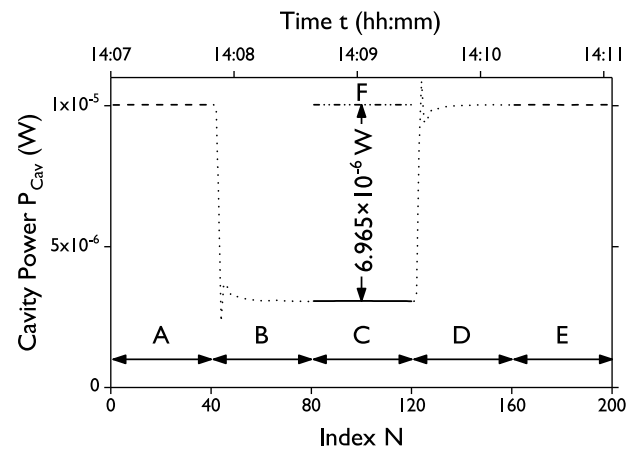

Fig. 3. Example of an optical power measurement using the absolute-cryogenic radiometer at $\lambda = 395$ nm. The measurement sequence has five steps: A, background before; B, settling period; C, data; D, settling period; E, background after; F, linear fit to A and E for background removal of C to determine the optical power.

power measurement. The resulting relative standard deviation of the measurement displayed in Fig. 3 was $\frac{\sigma_P}{P} = 0.05\%$.

C. Photodiodes

Finding large area (10 mm by 10 mm) photodiodes that were sufficiently resistant to ultraviolet irradiation [37], and at the same time did not exhibit large non-uniformities across their surface, turned out to be difficult. We tested many currently available detectors, but they were either not stable under ultraviolet irradiation or not uniform enough (see Fig. 4). We ended up using three diodes that were purchased previously and had not been used. Each of these diodes was a silicon photodiode with slightly different characteristics from the same manufacturer.

The photodiode qualification measurements were performed in the ultraviolet scale realization setup. The photodiodes were spatially scanned over an area of 12 mm by 12 mm in 0.6 mm steps at a wavelength of 350 nm. The diode was placed in the focus of the image of the optical system, where the beam is circular with a diameter of 2.1 mm (fourfold magnification of a 500 μm exit aperture; see Fig. 5). Then the resulting spatial data were plotted and evaluated. We were looking for photodiodes with a variation in the response of less than 1% across the surface.

To ensure that the photodiodes were detecting the same light field as the cavity in the ACR, each of the three photodiodes was installed in a 25.4 mm lens tube. Apertures of the same diameters were installed at the same distances as in the ACR.

Photodiodes are frequently mounted by inserting their anode and cathode pins into receptacles that are mounted within lens mounts. This method does not ensure that the photodiode is mounted reproducibly relative to the propagation direction of the light. We designed a mount for the photodiodes that completely restricts their motion and can be inserted into a 25.4 mm lens tube.

D. Data Acquisition

We operated five photodiodes in the experiment: a monitor detector (**M** in Fig. 1), the three photodiodes (**PD** in Fig. 1)
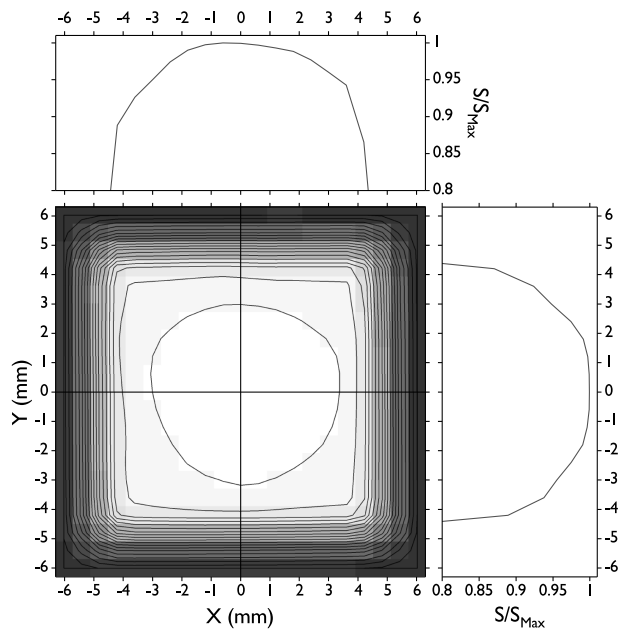
Fig. 4. Example of a photodiode spatial scan. The measured signal S was normalized by division with the maximum signal S_{Max}. This diode did not qualify, because of its non-uniformity.

being calibrated, and a photodiode in the wavelength calibration setup. The signal from the monitor diode was fed into a well characterized transimpedance amplifier, and the resulting voltage was collected with a high-accuracy digital voltmeter.

The signals from the other four photodiodes were first fed into a multiplexer, which allowed us to quickly switch between input channels. The output of the multiplexer was fed into the same model transimpedance amplifier as the monitor signal. The voltage output of the amplifier was read out with another digital voltmeter similar to the one used for the monitor data acquisition.

The data were acquired using the following method: The photodiode-under-test's signal and the monitor diode's signal were collected simultaneously. One of the three detectors was positioned into the beam coming from the monochromator. The shutter was closed, and $N = 100$ data points were collected as background. Then the shutter was opened, and another $N = 100$ data points were collected during the settling period. The last $N = 100$ data points were used to determine the signal. The mean of the first 100 data points was subtracted from the mean of the last 100 data points to remove the background, and the resulting voltage was multiplied with the transimpedance amplifier gain to determine the photocurrent.

E. Alignment

The exit aperture of the monochromator was imaged into the ACR with significant divergence; thus, alignment of the system and quality of the optical system became critical. To make sure the photodiodes were exposed to the same light field as the ACR-cavity, we installed the photodiodes in lens tubes with apertures mimicking the configuration of the ACR. The ACR, the three photodiodes-under-test, a 50.8 mm plane mirror, the holmium oxide target and photodiode, and a CCD camera were all installed on the same platform, which was mounted on a motorized x, y, z-stage (see Fig. 1).

In the first step of alignment, the 50.8 mm mirror was placed directly into the path of the light leaving the monochromator exit aperture at the closest distance allowed by the setup. The mirror was then adjusted so that the reflected light was collinear with the incoming light.

To allow for rapid alignment of the optical system, the two OAP mirrors were installed together prealigned on a single mount. Alignment of a single OAP in free space is challenging,
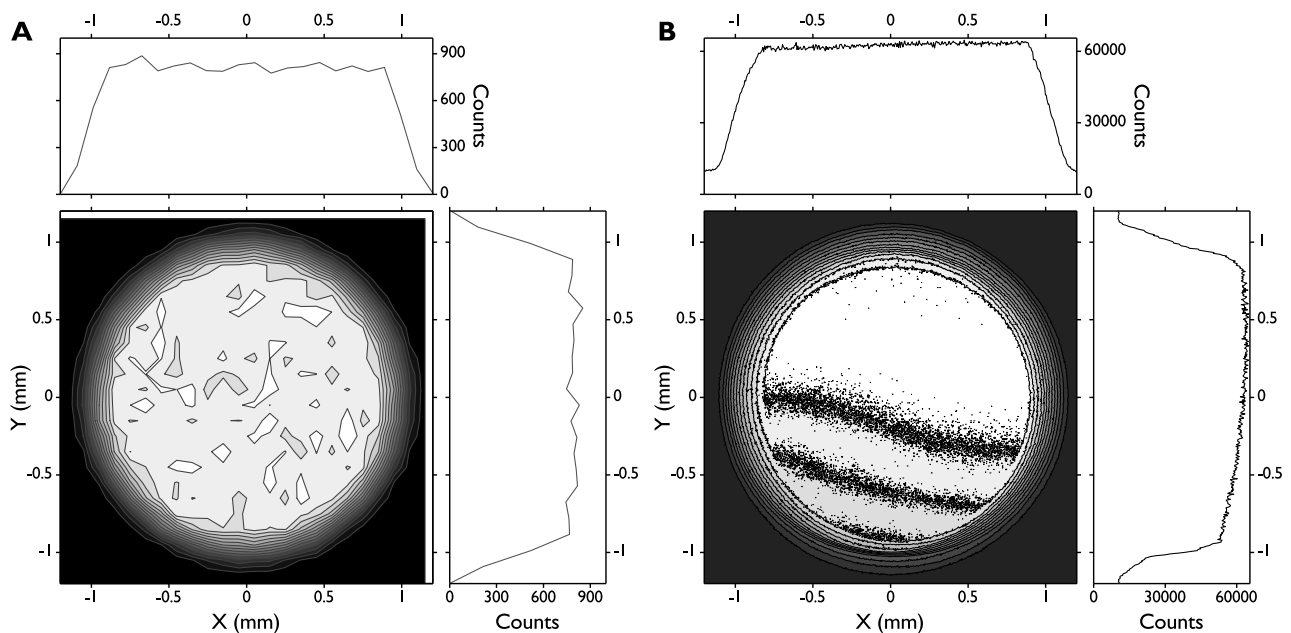

Fig. 5. A, ray tracing result for of the imaging system using SHADOW [39–41]. B Image of the 500 μm exit aperture of the monochromator using the two off-axis parabolic mirrors.

because of the 6 degrees of freedom (x, y, z, pitch θ_x, roll θ_y, and yaw θ_z) necessary for the adjustment and the difficulty of measuring collimation of a non-coherent beam, where a shearing-interferometer cannot be used. The most common method would be the use of a telescope and CCD camera. To perform the alignment in this system, a CCD camera was placed in the focus of the second OAP, and the mount was moved in three dimensions into the correct position. Then the 50.8 mm mirror was used to align the mount with the OAPs angularly, and then the CCD camera was used again to check the focus. This method leads to an image quality that closely resembles results using ray tracing (see Fig. 5). Once the transfer optical system had been aligned, the ACR and photodiodes had to be aligned angularly as well. For that, a custom-made reflector was slid over the ACR's snout, and the device was aligned until the reflected light was collinear with the incoming light. Then the photodiodes were aligned angularly using the same technique by reflecting light of their surfaces.

After the angular alignment had been completed, the spatial responses of the different components were mapped out in order to ensure that they were underfilled and to determine the optimal measurement positions.

F. Window Transmission

As can be seen in Fig. 1 the high vacuum of the ACR vacuum vessel was separated from the laboratory atmosphere by a high quality fused silica window. In order to derive the responsivity from an optical power and photocurrent measurement, the window transmission had to be taken into account. In order to measure the transmission in the actual spot that was illuminated, the spot had to be marked by sliding a plastic flange cap over the window when it was in the measurement position. Then the spot had to be marked on the cover as well as the orientation of the cover on the window and the window, because it was installed on a rotatable flange. The window transmission was measured before and after the measurement campaign.

Unfortunately, the window had to be removed and installed in a different location on the measurement platform for the window transmission measurement. The window was installed at the same distance from the second OAP mirror as it was in front of the ACR vacuum chamber. Using the plastic cap, it was positioned so that the same spot on the window was illuminated as in front of the ACR. Then a photodiode was installed in such a way that it was underfilled by the light and rotated by about 45°, so that no reflected light from the photodiode would disturb the measurement. The window transmission was determined using the same algorithm as in the wavelength calibration. At each wavelength λ, three measurements were performed: the signal and monitor background currents with and without the window, and with the shutter closed.

The transmittance $T(\lambda)$ was calculated by first subtracting the backgrounds collected with the shutter closed from the raw signal and monitor currents and then dividing the signal to monitor ratios measured with the window in place by the signal to monitor ratios collected without the window. This transmission scan was repeated several times, and the mean and standard deviations were calculated.

3. UNCERTAINTIES

The uncertainty in the irradiance calibration was evaluated following the methods of the Joint Committee for Guides in Metrology (JCGM) 100:2008 Guide to the Expression of Uncertainty in Measurement [32]. The components of uncertainty are divided into Type A and Type B components. Type A components were evaluated at the time of measurement by statistical analysis of the measurement results. Typical values were indicated in the present discussion. Type B components are discussed in some detail in the following section. The uncertainties given here are standard uncertainties, i.e., coverage factor $k = 1$.

The main source of type A statistical uncertainty stemmed from the noise floor of the ACR of ± 2 nW. At a reduced level, the noise in the photodiode current measurement also contributed to the statistical noise. The components of the combined relative standard uncertainty are listed in Table 1.

To account accurately for the wavelength uncertainty of a measurement, like, e.g., in the transmission or responsivity, the measured function of λ had to be numerically differentiated to calculate the sensitivity factor. In Fig. 6, the different uncertainty contributions are shown. The uncertainties in wavelength determination and transmission measurement were the largest contributors over the whole wavelength range.

The uncertainty resulting from the non-uniformity of the photodiodes and positioning inaccuracies was estimated numerically. Both the distribution of the light on the detector and the uniformity were modeled using two-dimensional Gaussian distributions. Assuming a positioning uncertainty of $\sigma_r = 0.1$ mm and a detector uniformity of better than 99%, the resulting relative uncertainty was 0.15%.

Stray-light or out-of-band radiation was assumed to be very small for a double monochromator. The relative standard uncertainty caused by stray-light was estimated to be 0.001% [4].

To estimate the influence of the spectral bandwidth, the spectral response of the monochromator was measured using a

Table 1.　Components of the Combined Relative Standard Uncertainty of Spectral Responsivity with a Coverage Factor of $k = 1$

Type A (random uncertainty)

	$\sigma_x / \langle X \rangle$ [%]
ACR power	0.02 to 2
Photodiode current	0.02 to 0.2

Type B (systematic uncertainty)

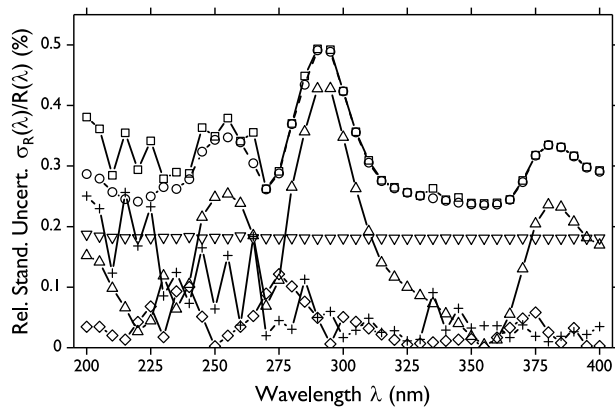|	$\sigma_x / \langle X \rangle$ [%]
Window transmission	<0.2
Wavelength scale	<0.45
Spectral bandwidth	<0.15
Diode uniformity and positioning	0.15
Stray-light	<0.001
Power measurements scale factor	0.013
Cavity absorptance	0.0002
Electrical non-equivalence	0.0006
Digital voltmeter	0.01
Transimpedance amplifier	0.01

Fig. 6. Wavelength dependence of the uncertainty contributions in the spectral responsivity measurement for detector-under-test #1. Total combined relative standard uncertainty $\sigma_R(\lambda)/R(\lambda)$ ($\square$), combined systematic relative standard uncertainty ($\bigcirc$), relative standard wavelength uncertainty $\sigma_\lambda(\lambda)/R(\lambda)$ ($\triangle$), relative standard transmission uncertainty $\sigma_T(\lambda)/R(\lambda)$ (∇), relative standard bandwidth uncertainty $\sigma_{\Delta\lambda}(\lambda)/R(\lambda)$ ($\diamond$), and random relative standard uncertainty ($+$).

high-resolution spectrometer. The full width at half-maximum of the monochromator response function for the 0.5-mm-diameter exit aperture was found to be between 3 nm and 3.5 nm. The measured monochromator response $M(\lambda)$ was numerically convoluted with the measured spectral responsivity $R(\lambda)$

and then compared to $R(\lambda)$ as an estimate of the uncertainty caused by the finite bandwidth [4,38].

Shaw and co-workers [12] reported the relative standard uncertainty components for the power measurement scale factor, the cavity absorptance, and electrical non-equivalence to be 0.013%, 0.002%, and 0.006%, respectively.

The relative standard uncertainty for the digital voltmeter and the transimpedance amplifier was estimated to be 0.01% for both [4].

The uncertainty analysis is summarized in Table 1 and Fig. 6.

4. RESULTS

The responsivity $R(\lambda)$ is given by the ratio of the photocurrent $I(\lambda)$ and the optical power $P(\lambda)$ [see Eq. (1)].

In this case, the power measured with the ACR, $P_{\text{ACR}}(\lambda)$, had to be corrected with the window transmission $T(\lambda)$,

$$R(\lambda) = \frac{I(\lambda)}{\frac{P_{\text{ACR}}(\lambda)}{T(\lambda)}} = \frac{I(\lambda) \cdot T(\lambda)}{P_{\text{ACR}}(\lambda)}. \tag{6}$$

The measurements displayed in Fig. 7 were performed using the following procedure. First a wavelength λ was selected, and the active position maintenance of the monochromator control software was enabled. Then the loop was started going through the following steps

1. Move to ACR position.
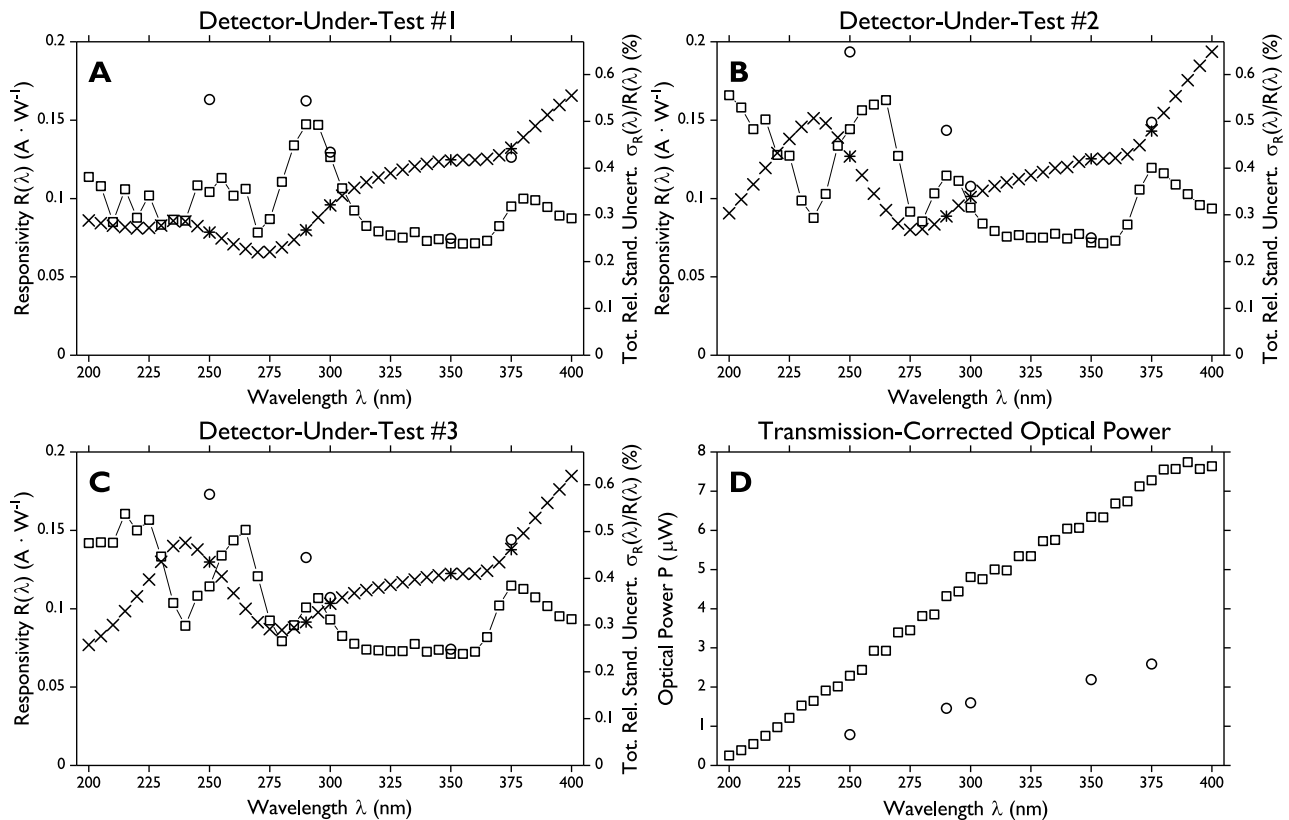2. Run the ACR and measure the optical power.

Fig. 7. A, spectral power responsivity of DUT1, measured with a 0.5 mm ($\times$) and 0.3 mm ($+$) exit apertures. Also shown are the total relative combined standard uncertainties for 0.5 mm ($\square$) and 0.3 mm ($\bigcirc$). B, same as A for DUT2. C, same as A for DUT3. D, measured transmission-corrected optical power in the ultraviolet scale realization setup using a 0.5 mm ($\square$) and a 0.3 mm ($\bigcirc$) exit aperture in the monochromator.

3. Move to photodiode 1 position.
4. Measure the current.
5. Move to photodiode 2 position.
6. Measure the current.
7. Move to photodiode 3 position.
8. Measure the current.
9. Go to step 1.

After several loops, the measurement was stopped, the wavelength was changed, and a new measurement was initiated. The raw data for each power and current measurement were stored on the data acquisition computer for later evaluation.

For example, at $\lambda = 250$ nm, we performed N = 10 sequential measurements. The measured optical power was $P = 2.288 \cdot 10^{-6}$ W with $\frac{\sigma_P}{\langle P \rangle} = 0.21\%$, the photocurrent for detector-under-test #1 was $I = 1.795 \cdot 10^{-7}$ A with $\frac{\sigma_I}{\langle I \rangle} = 0.031\%$, and the resulting responsivity $R = 0.0785$ A/W with $\frac{\sigma_R}{\langle R \rangle} = 0.20\%$. The results for three detectors-under-test are displayed in Fig. 7. We measured the spectral responsivity of the three test devices every 5 nm between 200 nm and 400 nm using a 500 μm exit aperture in the monochromator. After this measurement campaign was completed, we reduced the size of the exit aperture diameter to 300 μm and repeated the measurements at a few wavelengths to make sure that the ACR-cavity was underfilled. The results from this comparison agreed within the uncertainties we derived.

The laser-driven light source was stable within monitor signal uncertainty over short time spans. Because of the high stability over minutes, we did not use the monitor signal in our data reduction. The monitor data were collected, but their inclusion did not improve the results and would only have introduced another source of noise and random uncertainties.

5. CONCLUSION

We successfully determined the spectral power responsivity of three photodiodes in the wavelength range from 200 nm to 400 nm by comparing their current output to power measurements using an ACR. This novel approach was based on a laser-driven light source and a monochromator equipped with an absolute angular encoder. The combined relative standard uncertainty of the responsivity measurements was around or below 0.5% ($k = 1$) for the whole spectral range.

To eliminate further sources of uncertainty, absolute encoders should be installed on all motion stages. The measurement procedure would benefit from a scheme in which the window transmission can be measured _in situ_ without removing the window. If the throughput of the optical system could be improved significantly, the random uncertainties in the optical power and current measurements could be reduced.

Disclosures. The authors declare no conflicts of interest.

REFERENCES

1. S. W. Brown, G. P. Eppeldauer, and K. R. Lykke, "Facility for spectral irradiance and radiance responsivity calibrations using uniform sources," Appl. Opt. **45**, 8218–8237 (2006).
2. M. Schuster, S. Nevas, A. Sperling, and S. Völker, "Spectral calibration of radiometric detectors using tunable laser sources," Appl. Opt. **51**, 1950–1961 (2012).
3. R. Korde and J. Geist, "Quantum efficiency stability of silicon photodiodes," Appl. Opt. **26**, 5284–5290 (1987).
4. T. C. Larason and J. M. Houston, "Spectroradiometric detector measurements: ultraviolet, visible, and near-infrared detectors for spectral power," Special Report SP250-41 (NIST, 2008).
5. J. Campos, A. Corróns, A. Pons, P. Corredera, J. L. Fontecha, and J. R. Jiménez, "Spectral responsivity uncertainty of silicon photodiodes due to calibration spectral bandwidth," Meas. Sci. Technol. **12**, 1926–1931 (2001).
6. L.-P. Boivin, "Study of bandwidth effects in monochromator-based spectral responsivity measurements," Appl. Opt. **41**, 1929–1935 (2002).
7. A. Gamouras, A. D. W. Todd, É. Côté, and N. L. Rowell, "The development of the advanced cryogenic radiometer facility at NRC," J. Phys. Conf. Ser. **972**, 012014 (2018).
8. R. E. Poulson, "Test methods in spectrophotometry: stray-light determination," Appl. Opt. **3**, 99–104 (1964).
9. H. Rabus, V. Persch, and G. Ulm, "Synchrotron-radiation-operated cryogenic electrical-substitution radiometer as the high-accuracy primary detector standard in the ultraviolet, vacuum-ultraviolet, and soft-x-ray spectral ranges," Appl. Opt. **36**, 5421–5440 (1997).
10. P. Kuschnerus, H. Rabus, M. Richter, F. Scholze, L. Werner, and G. Ulm, "Characterization of photodiodes as transfer detector standards in the 120 nm to 600 nm spectral range," Metrologia **35**, 355–362 (1998).
11. P.-S. Shaw, K. Lykke, R. Gupta, T. O'Brian, U. Arp, H. White, T. Lucatorto, J. Dehmer, and A. Parr, "New ultraviolet radiometry beamline at the synchrotron ultraviolet radiation facility at NIST," Metrologia **35**, 301–306 (1998).
12. P.-S. Shaw, K. R. Lykke, R. Gupta, T. R. O'Brian, U. Arp, H. H. White, T. B. Lucatorto, J. L. Dehmer, and A. C. Parr, "Ultraviolet radiometry with synchrotron radiation and cryogenic radiometry," Appl. Opt. **38**, 18–28 (1999).
13. A. Gottwald, U. Kroth, M. Krumrey, M. Richter, F. Scholze, and G. Ulm, "The PTB high-accuracy spectral responsivity scale in the VUV and x-ray range," Metrologia **43**, S125–S129 (2006).
14. S. Horne, D. Smith, M. Besen, M. Partlow, D. Stolyarov, H. Zhu, and W. Holber, "A novel high-brightness broadband light-source technology from the VUV to the IR," Proc. SPIE **7680**, 76800L (2010).
15. H. Zhu and P. Blackborow, "DLS sheds light on analytical-sciences applications," Laser Focus World **47**, 53 (2011).
16. X. Ye, H. Zhu, M. Besen, and A. Cutler, "Vis-NIR spectral flatness improvement for Laser-Driven Light Sources (LDLS)," Proc. SPIE **10758**, 107580N (2018).
17. U. Arp, R. Vest, J. Houston, and T. Lucatorto, "Argon mini-arc meets its match: use of a laser-driven plasma source in ultraviolet-detector calibrations," Appl. Opt. **53**, 1089–1093 (2014).
18. U. Arp and R. Vest, "Use of a laser-driven plasma source in the ultraviolet spectral comparator facility," in _NEWRAD_ (2014), pp. 181–182.
19. J. M. Bridges and W. R. Ott, "Vacuum ultraviolet radiometry. 3: The argon mini-arc as a new secondary standard of spectral radiance," Appl. Opt. **16**, 367–376 (1977).
20. W. R. Ott, J. M. Bridges, and J. Z. Klose, "Vacuum-ultraviolet spectral-irradiance calibrations: method and applications," Opt. Lett. **5**, 225–227 (1980).
21. J. L. Lean, H. J. Kostkowski, R. D. Saunders, and L. R. Hughey, "Comparison of the NIST SURF and argon miniarc irradiance standards at 214 nm," Appl. Opt. **28**, 3246–3253 (1989).
22. J. E. Martin, N. P. Fox, and P. J. Key, "A cryogenic radiometer for absolute radiometric measurements," Metrologia **21**, 147–155 (1985).
23. N. P. Fox, "Radiometry with cryogenic radiometers and semiconductor photodiodes," Metrologia **32**, 535–543 (1995).

24. T. R. Gentile, J. M. Houston, J. E. Hardis, C. L. Cromer, and A. C. Parr, "National institute of standards and technology high-accuracy cryogenic radiometer," Appl. Opt. **35**, 1056–1068 (1996).

25. G. Eppeldauer and J. E. Hardis, "Fourteen-decade photocurrent measurements with large-area silicon photodiodes at room temperature," Appl. Opt. **30**, 3091–3099 (1991).

26. R. Korde and J. Geist, "Stable, high quantum efficiency, UV-enhanced silicon photodiodes by arsenic diffusion," Solid-State Electron. **30**, 89–92 (1987).

27. M. Czerny and A. F. Turner, "Über den astigmatismus bei Spiegelspektrometern," Z. Physik **61**, 792–797 (1930).

28. V. R. Weidner, R. Mavrodineanu, K. D. Mielenz, R. A. Velapoldi, K. L. Eckerle, and B. Adams, "Spectral transmittance characteristics of holmium oxide in perchloric acid solution," J. Res. Natl. Bur. Stand. **90**, 115–125 (1985).

29. J. C. Travis, J. C. Zwinkels, F. Mercader, A. Ruíz, E. A. Early, M. V. Smith, M. Noël, M. Maley, G. W. Kramer, K. L. Eckerle, and D. L. Duewer, "An international evaluation of holmium oxide solution reference materials for wavelength calibration, in molecular absorption spectrophotometry," Acta Chem. **74**, 3408–3415 (2002).

30. J. C. Travis, J. C. Acosta, G. Andor, J. Bastie, P. Blattner, C. J. Chunnilall, S. C. Crosson, D. L. Duewer, E. A. Early, F. Hengstberger, C. S. Kim, L. Liedquist, F. Manoocheri, F. Mercader, L. A. G. Monard, S. Nevas, A. Mito, M. Nilsson, M. Noël, A. C. Rodriguez, A. Ruíz, A. Schirmacher, M. V. Smith, G. Valencia, N. Van Tonder, and J. Zwinkels, "Intrinsic wavelength standard absorption bands in holmium oxide solution for UV/visible molecular absorption spectrophotometry," J. Phys. Chem. Ref. Data **34**, 41–56 (2005).

31. C. Palmer, *Diffraction Grating Handbook*, 8th ed. (MKS Instruments, Inc., 2020).

32. "Evaluation of measurement data—guide to the expression of uncertainty in measurement," in *Guide, Joint Committee for Guides in Metrology (JCGM)* (2008).

33. A. Haapalinna, P. Kärhä, and E. Ikonen, "Spectral reflectance of silicon photodiodes," Appl. Opt. **37**, 729–732 (1998).

34. Ö. Bazkir, "Determination of optical constants of silicon photodiode from reflectivity measurements at normal incidence of light," Opt. Laser Eng. **45**, 245–248 (2007).

35. M. Sildoja, F. Manoocheri, and E. Ikonen, "Reducing photodiode reflectance by Brewster-angle operation," Metrologia **45**, 11–15 (2008).

36. A. L. M. Zurita, J. C. Acosta, A. F. Turrión, and A. P. Aglio, "Photodiodes as optical radiation measurement standards," in *Photodiodes*, I. Yun, ed. (IntechOpen, 2012), Chap. 5.

37. U. Arp, P.-S. Shaw, R. Gupta, and K. R. Lykke, "Damage to solid-state photodiodes by vacuum ultraviolet radiation," J. Electron Spectrosc. Relat. Phenom. **144–147**, 1039–1042 (2005).

38. H. J. Kostkowski, J. B. Shumaker, and F. E. Nicodemus, "Self-study manual on optical radiation measurements: part 1–chapters 7, 8, and 9," NBS Technical Note 910-4 (National Bureau of Standards, 1979).

39. C. Welnak, P. Anderson, M. Khan, S. Singh, and F. Cerrina, "Recent developments in SHADOW," Rev. Sci. Instrum. **63**, 865 (1992).

40. F. Cerrina and M. S. del Rio, *Ray Tracing of X-Ray Optical Systems* (Mc Graw Hill, 2009), Vol. **V**, Chap. 35.

41. M. Sanchez del Rio, N. Canestrari, F. Jiang, and F. Cerrina, "SHADOW3: a new version of the synchrotron X-ray optics modelling package," J. Synchrotron Radiat. **18**, 708–716 (2011).